

Article

Highly Sensitive and Selective MEMS Gas Sensor Based on WO₃/Al₂O₃/Graphite for 2-Chloroethyl Ethyl Sulfide (2-CEES) Detection

Liangpan Yang^{1,†}, Wangze Cheng^{1,†}, Wenlong Yan¹, Li Wen^{2,*}, Changyue Xia^{1,3}, Chuang Sun^{1,3}, Doumeng Hu^{1,*}, Yunong Zhao¹, Xiaohui Guo^{1,3}, Wei Zeng^{1,3} and Siliang Wang^{1,3}

¹ Information Materials and Intelligent Sensing Laboratory of Anhui Province & Industry-Education-Research Institute of Advanced Materials and Technology for Integrated Circuits, Anhui University, Hefei 230601, China; ylp@ahu.edu.cn (L.Y.); wb22201006@stu.ahu.edu.cn (W.C.); p20301217@stu.ahu.edu.cn (W.Y.); p21301131@stu.ahu.edu.cn (C.X.); p21301240@stu.ahu.edu.cn (C.S.); zhaoyun@ahu.edu.cn (Y.Z.); guoxh@ahu.edu.cn (X.G.); zengwei@ahu.edu.cn (W.Z.); wangsl@ahu.edu.cn (S.W.)

² Center for Nanoscale Characterization & Devices (CNCD), School of Physics and Wuhan National Laboratory for Optoelectronics (WNLO), Huazhong University of Science and Technology (HUST), Wuhan 430074, China

³ East China Institute of Photo-Electron ICs, Suzhou 215163, China

* Correspondence: d202080082@hust.edu.cn (L.W.); hdm@ahu.edu.cn (D.H.)

† These authors contributed equally to this work.

Abstract: The detection and monitoring of toxic and harmful gases play a vital role in environmental protection, human health, and industrial and agricultural production. However, it is still challenging to develop gas sensors for the detection of toxic and harmful gases with high sensitivity, good recovery and excellent selectivity. In this study, WO₃/Al₂O₃/graphite composite materials were used for an MEMS 2-CEES gas sensor (dichlorodiethyl sulfide simulation), and the corresponding sensing properties were explored. The experimental results show that when the working temperature is 340 °C, the response of the sensor to 2-CEES gas with a concentration of 5.70 ppm is 69%, the response time is 5 s and the recovery time is 42 s. The sensor also has the advantages of long-term stability and high selectivity. Furthermore, the MEMS gas sensor array based on WO₃/Al₂O₃/graphite composite materials has been achieved and also exhibits excellent sensing performance. Overall, this study provides a strategy for realizing high-performance dichlorodiethyl sulfide gas sensors.

Keywords: MEMS; gas sensor; 2-CEES; long-term stability; high selectivity



Citation: Yang, L.; Cheng, W.; Yan, W.; Wen, L.; Xia, C.; Sun, C.; Hu, D.; Zhao, Y.; Guo, X.; Zeng, W.; et al. Highly Sensitive and Selective MEMS Gas Sensor Based on WO₃/Al₂O₃/Graphite for 2-Chloroethyl Ethyl Sulfide

(2-CEES) Detection. *Chemosensors*

2024, 12, 5. <https://doi.org/10.3390/chemosensors12010005>

Academic Editor: Pi-Guey Su

Received: 5 November 2023

Revised: 26 December 2023

Accepted: 28 December 2023

Published: 30 December 2023



Copyright: © 2023 by the authors. Licensee MDPI, Basel, Switzerland. This article is an open access article distributed under the terms and conditions of the Creative Commons Attribution (CC BY) license (<https://creativecommons.org/licenses/by/4.0/>).

1. Introduction

According to the mechanism of toxicity in humans, toxic and harmful gases are classified into blister agents, nerve agents, blood agents, and pulmonary agents [1]. As the common blistering agent, dichlorodiethyl sulfide is notorious for harming human health, such as the erythema, edema, blistering, erosion, etc. [2]. In order to prevent the potential harm to human health, the sensitive detection of toxic and harmful gases is required. As the testing of dichlorodiethyl sulfide at laboratory levels is dangerous, experimental studies are usually performed with less toxic chemicals, among which 2-chloroethyl ethyl sulfide (2-CEES) is used as a simulant for dichlorodiethyl sulfide [3,4].

So far, there have been some well-developed technologies for the detection of toxic and harmful gases. These technologies include gas chromatography-mass spectrometry (GC-MS) [5], proton-transfer-reaction mass spectrometry (PTR-MS) [5], ion mobility spectrometry (IMS) [6], Raman spectroscopy [7], surface acoustic wave sensors (SAWs) [8], quartz-crystal microbalance sensors (QCMs) [9] and colorimetric tubes [10]. However, they have certain defects such as valuableness, low response and sensitivity, poor reversibility, etc. By comparison, gas sensors based on metal oxide semiconductors have advantages of low cost, portability, fast response time and easy fabrication [11–13].

There are a few semiconductor metal oxide sensors that have also been reported in the previous literature for the detection of 2-CEES gas. For example, Zheng et al. reported the detection of 2-chloroethyl ethyl sulfide (2-CEES) by crosslinked WO_3 nanonet. But the recovery time of the gas sensor to 2-CEES gas with a concentration of 5 ppm is up to 162 s [14]. Li et al. reported that hierarchical Fe_2O_3 nanotube arrays were synthesized by an in situ solvothermal method for the detection of 2-CEES gas. However, the recovery time of the gas sensor is 190 s [15]. Yang et al. reported that a hierarchical core-shell ZnFe_2O_4 microspheres gas sensor was fabricated for the detection of 2-CEES. However, the recovery time of the gas sensor for 1 ppm 2-CEES is as long as 546 s [13]. As is well known, the selectivity and response/recovery time of the sensors are important indicators for their practical application. Therefore, the goal of this paper is to improve the sensing properties of the above semiconductor metal oxide gas sensors, such as improving the selectivity to 2-CEES gas and shortening the response and recovery time.

Tungsten oxide (WO_3) is a typical n-type metal oxide, and its nanostructures are widely used as gas-sensing materials because of its superior physical and chemical properties [16]. In view of this, $\text{WO}_3/\text{Al}_2\text{O}_3$ /graphite composite materials were prepared by high-temperature sintering and mechanical mixing, and the $\text{WO}_3/\text{Al}_2\text{O}_3$ /graphite gas sensor for the detection of 2-CEES was achieved in this study. The addition of graphite and Al_2O_3 can achieve the following advantages. Graphite not only has a very large theoretical specific surface area ($2630 \text{ m}^2/\text{g}$) but also has a high electrical conductivity so that the added graphite can provide a very large gas induction area per unit volume and effectively adsorb a large number of gas molecules [17]. In addition, the added Al_2O_3 can generate more gas interaction centers on the surface of WO_3 and improve adhesion and stability [18,19]. The experimental results show that the gas sensor exhibits excellent sensing performance. More importantly, the response to 5.70 ppm 2-CEES was much higher than that of NH_3 , acetone and acetonitrile, showing good selectivity. In order to demonstrate the practical application, a gas sensor array composed of $\text{WO}_3/\text{Al}_2\text{O}_3$ /graphite was prepared based on MEMS microprocessing technology. This sensor array also has a high response to 2-CEES. Therefore, this work may provide an effective strategy for detecting dichlorodiethyl sulfide due to the excellent gas-sensing performance of the sensor for 2-CEES gas.

2. Experimental Procedure

2.1. Chemical Reagent

All chemicals for this study were used as received without further purification. Acetone ($\text{C}_3\text{H}_6\text{O}$), ammonia ($\text{NH}_3(\text{aq})$) and ethanol ($\text{C}_2\text{H}_5\text{OH}$) were purchased from Sinopharm Sinopharm Chemical Reagent Co., Ltd., Shanghai, China. 2-Chloroethyl ethyl sulfide ($\text{C}_4\text{H}_9\text{ClS}$), acetonitrile ($\text{C}_2\text{H}_3\text{N}$) and tungsten oxide (WO_3 , average particle size < 100 nm) were purchased from Shanghai Macklin Biochemical Co., Ltd., Shanghai, China. Aluminum oxide (20 nm) was purchased from Shanghai D&B Biological Science and Technology Co., Ltd., Shanghai, China.

2.2. Materials Synthesis

First, WO_3 and Al_2O_3 were ground and mixed uniformly in a mortar. Then, the above mixed materials were put into a muffle furnace and calcined at 110 °C, 600 °C and 700 °C for 1 h in sequence. Then, the above-prepared materials and graphite were stirred in ethanol/deionized water (volume fraction 5:1) for 24 h and finally dried in an oven at 60 °C for 24 h. The samples with Al_2O_3 mass accounting for 2, 4, 8 and 12 wt. % of the total mass of Al_2O_3 and WO_3 were named S1, S2, S3 and S4, respectively.

2.3. Characterization

The morphology and structure of the sensing materials were characterized by transmission electron microscope (TEM, JEM-2100, JEOL, Tokyo, Japan), scanning electron microscopy (SEM, S-4800, Hitachi, Hitachi City, Japan), and X-ray diffraction (Japan; XRD, SmartLab, 9 KW, Rigaku, Tokyo, Japan).

2.4. Gas-Sensor Fabrication and Gas-Sensing System

Grind the sample in deionized (DI) water into a uniform slurry in an agate mortar, then brush it onto a ceramic tube to form a uniform film, and dry it at 180 °C for 40 min. Then, weld the ceramic tube onto the hexagonal base. The nickel chromium alloy spiral heating wire passing through the ceramic tube is used to adjust the working temperature. The gas-sensing performance of the sensor was tested by the static volume method. The sensor is tested in a sealed chamber of 18 L, and when the resistance of the sensor is stable, the calculated target gas or liquid is injected into the chamber through a micro-syringe, which is quickly and evenly distributed in the test chamber under the drive of a fan. This is a simple and easy method, and it is widely used in the configuration of standard gases. A commercial gas sensor tester (WS-30B) is used to test the gas-sensing performance of the sensor. The whole test system was placed in the fume hood equipped with a dehumidifier. The relative humidity of the experimental environment was controlled at 35% RH. The measurement circuits contain a sensor resistance (R_S), an adjustable standard resistance (R_L), and DC voltage source (V_C). The working temperature of the sensor is regulated by the heating voltage (V_H), and the formula $R_S = (V_C - V_{\text{output}})R_L/V_{\text{output}}$ is used for calculating the sensor resistance. The following formula $C = \frac{22.4 \times \varphi \times \rho \times V_1}{M \times V_2} \times 1000$ is used to calculate the volume of injected liquid organic compounds, where M (g/mol), ρ (g/mL) and V_1 (μL) are, respectively, the molecular weight, density and volume of the liquid organic compounds, V_2 (L) is the volume of the gas chamber, C (ppm) is the target gas concentration, and φ is the target gas volume fraction. The response of the sensor is defined as: $\text{response (\%)} = (R_a - R_g)/R_a \times 100$, where R_a and R_g are the resistance in air and target gas. Response time is defined as the time required for the resistance to reach 90% of the stable resistance after the sensor contacts the gas under test. Recovery time is defined as the time required for the resistance value to decrease to 90% of the stable resistance after the sensor is exposed to air.

3. Results and Discussion

3.1. Structure and Measurement Circuit of the Sensor

The ceramic tube shell packaging is used to study the sensing characteristics of sensitive materials and the gas sensor. Figure 1a shows the photograph of the gas sensor that consists of a ceramic tube coated with sensing materials and a base with six probes. The measurement circuit of the gas sensor tester containing a sensor resistance (R_S), an adjustable standard resistance (R_L) and a DC voltage source (V_C) is shown in Figure 1b. The rated measurement voltage was added to both ends of the circuit, and then the voltage V_C at both ends of R_L can be measured, and the resistance of R_S can be calculated. To obtain sensor responses under different gases by real-time recording of R_S , the working temperature is crucial for the gas-sensing performance of metal oxides sensor. Thus, the working temperature of the sensor is regulated by the provided heating voltage (V_H) applying to the nickel chromium alloy. Figure 1c shows the structural diagram of the gas sensor that is welded to the base by platinum wires protruding from the gold electrodes at the ends of the ceramic tube.

3.2. Structure and Morphology

The microstructure of tungsten oxide, graphite and alumina oxide and the as-prepared composite S2 were examined by XRD, as shown in Figure 2a. The characteristic diffraction peaks at 23.55°, 34.11° and 49.88° can correspond well to the (020), (202) and (400) planes of WO_3 nanoparticles, respectively, and they can be indexed to the structure of WO_3 (JCPDS No.83-0950). No other secondary phases or impurity peaks were observed. This indicates the high purity of the synthetic $\text{WO}_3/\text{Al}_2\text{O}_3$ /graphite composite materials. To further understand the surface morphologies of the synthesized samples, their surface morphologies were characterized by scanning electron microscopy (SEM), as shown in Figures 2b and S1. As can be seen from the figures, the WO_3 and Al_2O_3 nanoparticles are tightly attached to the graphite sheets. But with the increase in the Al_2O_3 nanoparticle con-

tent, Al_2O_3 nanoparticles will also attach to the surface of WO_3 and agglomerate together. The phenomenon of agglomeration is not conducive to the gas-sensing performance, which indirectly indicates that the content of Al_2O_3 nanoparticles in the composites will have an optimal value.

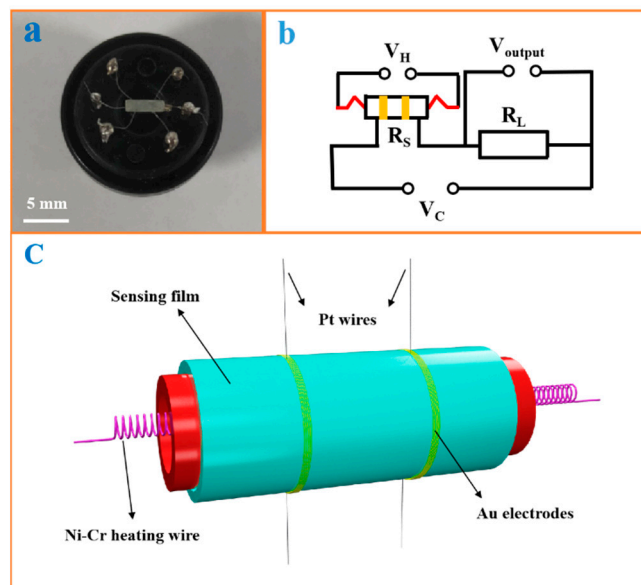


Figure 1. The gas sensor used in the experiments: (a) physical photo, (b) measurement circuit and (c) schematic diagram of the sensor configuration.

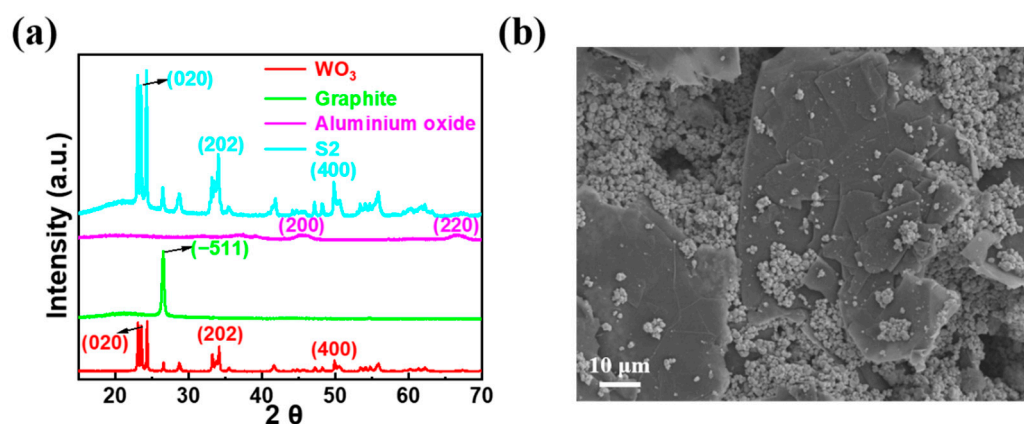


Figure 2. Characterization of sample S2. (a) The XRD pattern and (b) SEM image of sample S2.

The shape and size of the raw materials and synthesized sample were probed using a transmission electron microscope (TEM), as shown in Figure 3. As shown in Figure 3a, WO_3 is in the shape of nanoparticles with diameters ranging from tens to hundreds of nanometers. Figure 3b is a TEM image of Al_2O_3 . It can be seen from the figure that the Al_2O_3 nanoparticles are tiny and aggregated together. Figure 3c is a TEM image of graphite. It can be seen from the figure that graphite is a multi-layer flake structure. The inset of Figure 3c shows the selected area electron diffraction (SAED) of the graphite, showing the polycrystalline diffraction ring. Figure 3d is the TEM image of the S2 sample. The figure reflects that the WO_3 nanoparticles and Al_2O_3 nanoparticles are attached to the surface of the graphite. To further confirm the distribution of WO_3 , Al_2O_3 , and graphite in the S2 sample, the energy-dispersive spectrometer (EDS) was used, and the results are shown in Figure 3e–i. It can be seen from the figures that the elements of Al, O, W and C are dispersed uniformly, which indicates that WO_3 nanoparticles and Al_2O_3 nanoparticles are evenly mixed and evenly distributed on the surface of graphite.

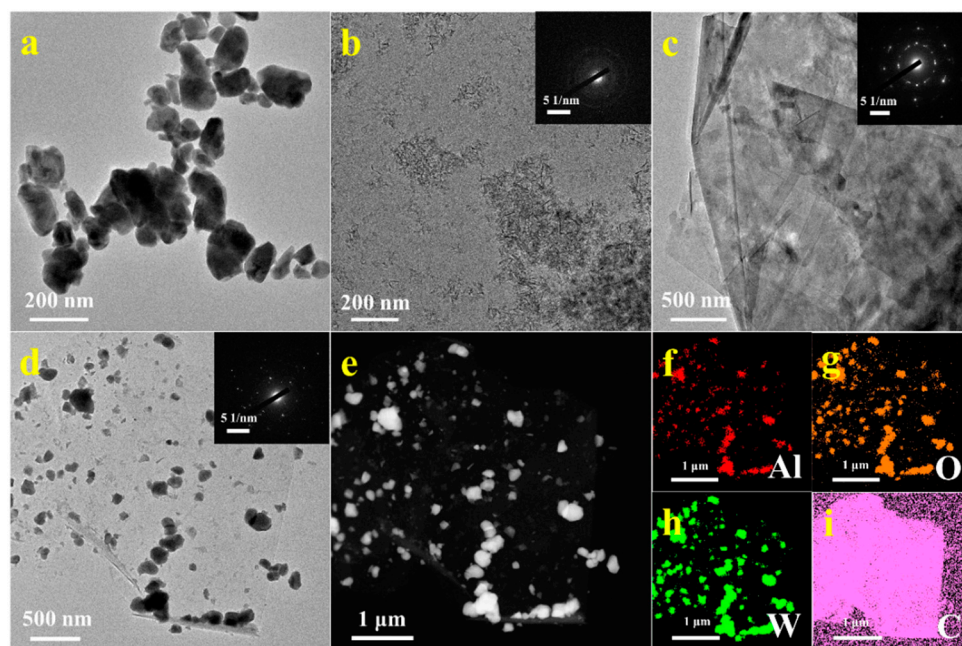


Figure 3. TEM images of WO_3 , Al_2O_3 , graphite and S2 sample. (a) The TEM image of WO_3 nanoparticles. (b) The TEM image of Al_2O_3 nanoparticles. (c) The TEM image of graphite. (d) The TEM image of sample S2. (e) The STEM image of sample S2. (f–i) Corresponding elemental mapping images of (f) Al, (g) O, (h) W, and (i) C.

3.3. Gas-Sensing Properties

To select the optimum additive amount of Al_2O_3 and operating temperature, the gas-sensing properties of the sensors with different additive amounts of Al_2O_3 were tested at different operating temperatures. As shown in Figure 4a and Figure S2, the sensor based on sample S2 under 5.70 ppm 2-CEES exhibits the greatest response at each operating temperature. It can also be seen from the figure that the response of the sensor based on sample S2 increases with the increase in the working temperature at the beginning, and when the response reaches the maximum value, it decreases with the further increase in the working temperature. This phenomenon may be explained as follows. When the working temperature is low, water molecules in the air will be adsorbed to the surface of the sensing material, which hinders the interaction between oxygen ions on the surface active sites of the sensing material and 2-CEES gas molecules [15]. When the operating temperature increases, the oxidation rate and gas diffusion coefficient will be increased, so the response will increase. The response of the sensor is maximized when the interaction rate of the 2-CEES gas is equal to the diffusion rate of the 2-CEES gas [20]. However, as the operating temperature further increases, insufficient atmospheric oxygen adsorbed on the sensor surface results in insufficient sensing sites on the sensing material surface, so the response begins to degrade [21].

Next, the response time and recovery time of the sensor based on sample S2 were studied, and the response time and recovery time to 5.70 ppm of 2-CEES at different temperatures are shown in Table 1. It can be seen that the higher the operating temperature, the shorter the response time and recovery time. This is because the higher the operating temperature, the stronger the adsorption and desorption ability of the gas on the sensor surface. Next, the selectivity of the sensor based on sample S2 was investigated. Figure 4b and Figure S3 exhibit the sensing responses of the S2 sensor to 5.70 ppm of 2-CEES and interfering gases (ammonia, ethanol, acetone and acetonitrile) at different temperatures. As can be seen from the figure, when the operating temperature is 260 °C, 300 °C, 340 °C and 440 °C, the response to ammonia, ethanol and acetonitrile is relatively low and changes little, and the response to 5.70 ppm 2-CEES was much higher. However, as the working

temperature increases, the response to acetone is improved. Therefore, to sum up, the optimal operating temperature of the sensor based on sample S2 is 340 °C. At this time, the response to 2-CEES gas with a concentration of 5.70 ppm was 69%. The response of 2-CEES is almost 6 times higher than that of ammonia and ethanol, 3 times higher than that of acetone and 70 times higher than that of acetonitrile. The response time and recovery time of the sensor based on sample S2 to 5.70 ppm 2-CEES gas were 5 s and 42 s, respectively, as shown in Figure 4c. The sensing response of the sensor to 0.10 ppm 2-CEES at the temperature of 340 °C is shown in Figure 4d. When 0.10 ppm 2-CEES is injected, the S2 sensor has 27% response, indicating that the sensor can detect 2-CEES gas with low concentration. This helps its application in real life to detect 2-CEES gas and can detect the leakage of 2-CEES gas as soon as possible.

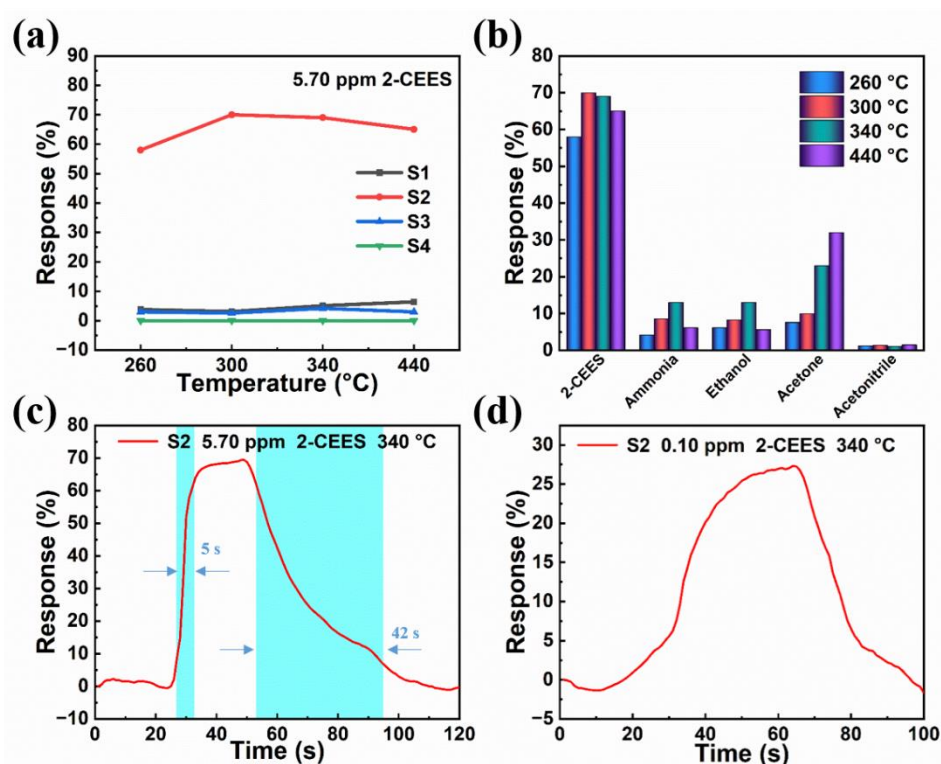


Figure 4. Gas-sensing performance of the sensors. (a) The relationship between response and temperature for 2-CEES. (b) The responses of the S2 sensor to 2-CEES and interfering gases with a concentration of 5.70 ppm under different temperatures. (c) The response and recovery time of the S2 sensor to 2-CEES (5.70 ppm) at the temperature of 340 °C. (d) The response of the S2 sensor to 2-CEES (0.10 ppm) at the temperature of 340 °C.

Table 1. The sensor response, response time and recovery time of the S2 sensor to 5.70 ppm of 2-CEES gas at different temperatures.

Temperature	Response	Response Time	Recovery Time
260 °C	58%	17 s	170 s
300 °C	70%	12 s	142 s
340 °C	69%	5 s	42 s
440 °C	65%	4 s	12 s

The response–recovery curves of the sensor based on sample S2 toward different 2-CEES gas concentrations in a range of 0.10–11.40 ppm are shown in Figure 5a. It can be seen from the figure that the response increased with the increment of 2-CEES gas concentration. This indicates that the sensor has good response recovery characteristics.

The linear dependence curve of the response on the gas concentration was also studied (Figure 5b). The initial response increased with increasing 2-CEES gas concentration, and the response tended to saturate when the 2-CEES gas concentration exceeded 3.10 ppm. This shows that the sensor has a relatively wide detection range. A dynamic response diagram of the reproducibility and stability of the sensor is shown in Figure 5c,d. At the end of each cycle, the resistance of the sensor tends to return to its original appearance. Figure 5c shows that the sensor exhibits good repeatability for 5.70 ppm 2-CEES at a heating temperature of 340 °C. The gas-sensitive performance of the sensor was tested for 6 consecutive days, and the results showed excellent stability. The response of the sensor to 2-CEES gas was maintained near 69% despite some fluctuations, as shown in Figure 5d. The sensor based on the S2 sample has good repeatability and long-term stability, which shows the application value of detecting dichlorodiethyl sulfide gas. To demonstrate the superiority of the developed sensor, the gas-sensing performances to 2-CEES gas between this work and those reported in previous publications were compared (Table 2), and the corresponding comparison results demonstrate that the $\text{WO}_3/\text{Al}_2\text{O}_3/\text{graphite}$ sensor exhibits high response, low working temperature, and it also shows fast response and recovery time. Therefore, all these results confirm that the $\text{WO}_3/\text{Al}_2\text{O}_3/\text{graphite}$ are promising gas-sensing materials for dichlorodiethyl sulfide gas detection in practical applications.

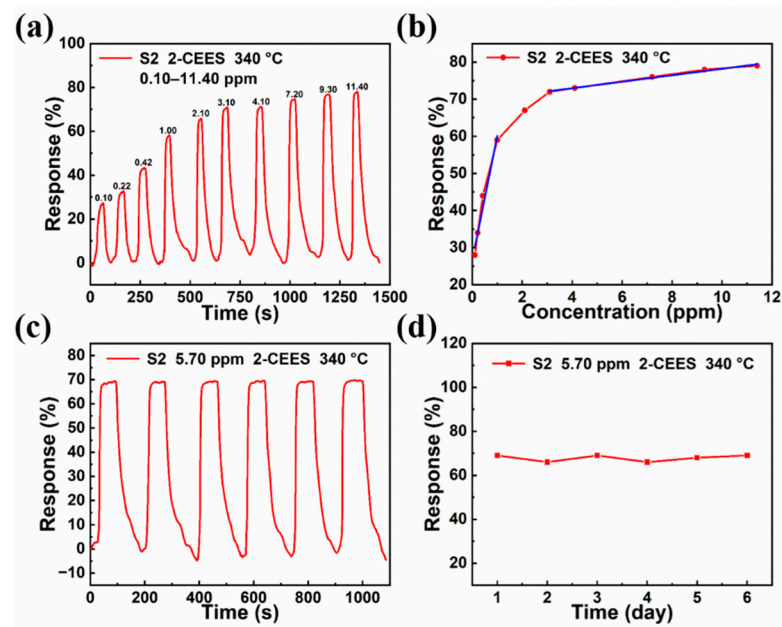


Figure 5. Gas-sensing performance of the sensor based on sample S2. (a) The response–recovery curves of the S2 sensor to 0.10, 0.22, 0.42, 1.00, 2.10, 3.10, 4.10, 7.20, 9.30 and 11.40 ppm of 2-CEES gas at temperature of 340 °C. (b) The linear dependence relation of the response of the sensor to different concentrations of 2-CEES gas at a temperature of 340 °C, the blue lines are the fitted linear curves. (c) The response repeatability of the sensor toward 2-CEES gas for 6 times cycle test. (d) The sensing response of the sensor to 5.70 ppm of 2-CEES at a temperature of 340 °C under continual 6 days testing.

In order to better apply a $\text{WO}_3/\text{Al}_2\text{O}_3/\text{graphite}$ gas sensor to detect dichlorodiethyl sulfide gas in real life, the MEMS chip array was applied. The structure diagram of the MEMS gas sensor chip is shown in Figure 6a. It can be seen that the gas-sensitive materials are loaded in the middle of the MEMS chip, and four Pt electrodes are connected to the ends. Some platinum electrodes are used for heating, while others are used for information collection. Figure 6b,c clearly show the planar SEM image of the MEMS micro-heating chip. After the gas-sensitive materials are loaded in the heating plates and then connected with external circuits by wire bonding, the MEMS gas sensor array is achieved. As shown

in Figure 6d, the MEMS gas sensor array testing system with ten test channels has been developed, and the gas sensors in each channel of the system can be tested under various types of gases. Next, to verify the consistency of the MEMS gas sensor array, we selected a sensor randomly for gas detection, and the response of the gas sensor to 2-CEES gas at a concentration of 5.70 ppm was measured at an optimal operating temperature of 340 °C. The response to various interfering gases, such as ammonia, ethanol and acetone, at the same concentration of 5.70 ppm under an operating temperature of 340 °C, are shown in Figure 7. As can be seen from Figure 7a, the single channel MEMS gas sensor has a high response to 2-CEES gas with a concentration of 5.70 ppm, and it has a rapid response and recovery. At the same time, it can be seen from Figure 7b, c and d that there was almost no response to ammonia and ethanol, and the response to acetone was much smaller than that to 2-CEES, which shows that the randomly selected MEMS gas sensor has good selectivity. These above experimental results indicate that sample S2's gas-sensing material can be well applied in MEMS chips for detecting dichlorodithyl sulfide gas.

Table 2. Comparison of gas-sensing characteristics of the S2 sensor with those reported in the literature.

Materials	Temperature	Response	Response Time	Recovery Time	Ref.
WO ₃ /Al ₂ O ₃ /gra-phite	340 °C	69% #	5 s	42 s	This work
Pt-CdSnO ₃ thin film	300 °C	33.46 *	8 s	125 s	[22]
Al-doped ZnO NPs	500 °C	954 #	2 s	127 s	[23]
Sm ₂ O ₃ doped SnO ₂ NPs	200 °C	540 #	50 s	1200 s	[24]
Ru-CdSnO ₃ thin film	350 °C	62.12 ^	5 s	185 s	[25]
crosslinked WO ₃ nanonets	217 °C	58 ^	1 s	181 s	[14]

The response calculation formula is as follows: $R^{\#}(\%) = (R_a - R_g)/R_a \times 100$; $S_{\#} = R_a/R_g$; $S^* = (G_g - G_a)/G_a$; $S^{\cdot} = (I_g - I_a)/I_a$. R_a and R_g are, respectively, the resistances in the air and in the test gas atmosphere. G_a and G_g are, respectively, the conductance in the air and in a target simulant medium. I_a and I_g are, respectively, the currents in the air and in the presence of simulant.

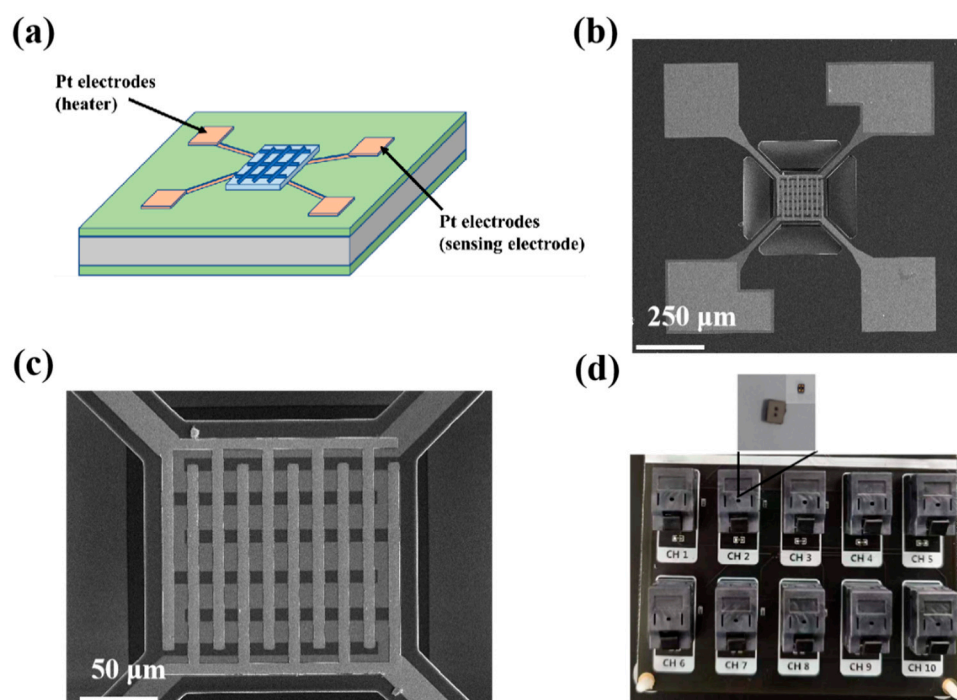


Figure 6. The MEMS-based 2-CEES gas sensor used in the experiments: (a) Schematic diagram of MEMS chip. (b,c) SEM images of the planar view of MEMS chip. (d) Schematic diagram of MEMS sensor array, the vignette is the enlarged photograph of the gas sensor.

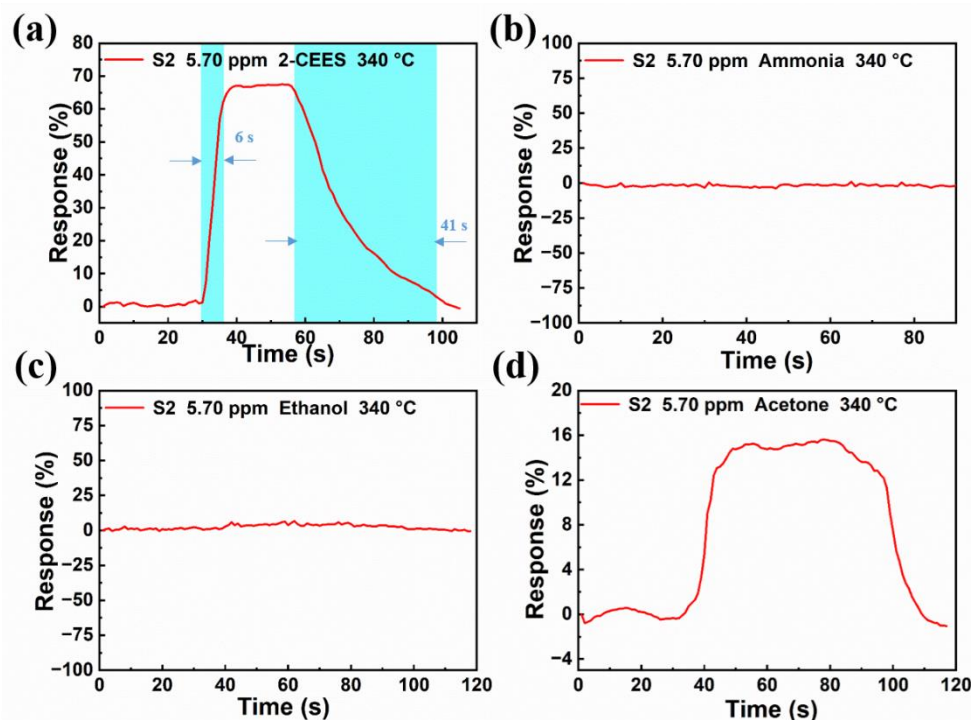


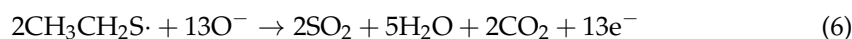
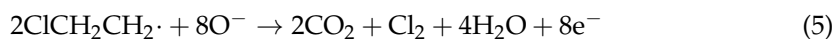
Figure 7. The response of MEMS-based gas sensor to 5.70 ppm of 2-CEES gas, ammonia, ethanol, and acetone. (a) 2-CEES gas. (b) ammonia. (c) ethanol. (d) acetone.

3.4. Sensing Mechanism

The adsorption and desorption properties of gases near the surface of sensing materials influence the resistance of sensing materials [26–29]. A depletion layer theory can be used for the explanation of the gas-sensing mechanism. When the sensor is placed in a clean air atmosphere without 2-CEES, a lot of oxygen is adsorbed on the sensor surface, and then it forms O_2^- , O^- and O^{2-} by reacting with the electrons transferred from the surface of the sensing materials [30,31]. The concentration of conduction band electrons in the sensing material decreases, an electron depletion layer is formed on the surface, and the resistance of the sensor increases. The reactions are described by Equations (1)–(4) [32].



Subsequently, at a certain temperature, the sensor is transferred to the 2-CEES atmosphere, and 2-CEES is rapidly decomposed into $ClCH_2CH_2\cdot$ and $\cdot SCH_2CH_3$. Due to the strong electrophilic properties of Cl and S, when they are adsorbed on the surface of the sensing material, they will react with O^- , are quickly oxidized and release a large number of electrons. The reactions are described by Equations (5) and (6). These free electrons will be transferred to the conduction band of the sensing material. The concentration of free electrons in the conduction band increases, resulting in the decrease in the depletion layer and the corresponding decrease in the resistance of the sensing material [33], as shown in Figure 8.



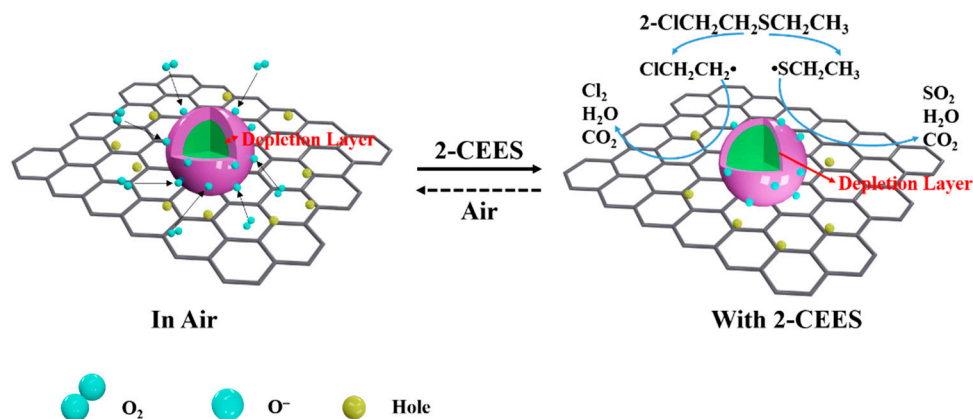


Figure 8. Response mechanism of $\text{WO}_3/\text{Al}_2\text{O}_3/\text{graphite}$ sensor for 2-chloroethyl ethyl sulfide (2-CEES) detection.

The process of Al_2O_3 distribution in WO_3 increases the specific surface area of WO_3 , generates more gas interaction centers on the surface of WO_3 , and improves adhesion and stability. WO_3 distributed with Al_2O_3 still retains the n-type semiconductor properties of undistributed WO_3 . The incorporation of Al_2O_3 can introduce more gas adsorption active sites for WO_3 . When the content of Al_2O_3 particles is low, the distribution has only a slight effect on WO_3 . With the increase in the content of Al_2O_3 particles, the adsorption of 2-CEES increases. However, with the continued incorporation of Al_2O_3 particles, the aggregation of Al_2O_3 particles will reduce the number of active sites (as shown in Figure S1b,c), and the adsorption capacity of the material for 2-CEES will decrease. Therefore, S2 can be used to obtain the maximum gas-sensitive property. The addition of graphite can increase the specific surface area of the sensing material, provide more interface contact and thus lead to more gas adsorption and a higher carrier mobility of sensing materials [34].

4. Conclusions

In this study, $\text{WO}_3/\text{Al}_2\text{O}_3/\text{graphite}$ nanocomposites were obtained with a simple high-temperature sintering and mechanical mixing. Compared with the sensors with different Al_2O_3 contents, the sensor with Al_2O_3 content of 4 wt. % exhibited the best gas-sensing characteristics. Experimental results show that when the working temperature is 340°C , the response time to 2-CEES gas with a concentration of 5.70 ppm is 5 s, the recovery time is 42 s and the response is 69%. The response of 2-CEES is almost 6 times higher than that of ammonia and ethanol, 3 times higher than that of acetone and 70 times higher than that of acetonitrile, which shows that this sensor exhibits an excellent selectivity to several possible interferences. The sensor also has the advantages of good repeatability and stability, and it can detect low-concentration 2-CEES gas. The MEMS gas sensor array based on $\text{WO}_3/\text{Al}_2\text{O}_3/\text{graphite}$ composite materials also exhibits excellent sensing performance. Considering the simple synthesis method and excellent gas-sensing performance, there is no doubt that $\text{WO}_3/\text{Al}_2\text{O}_3/\text{graphite}$ prepared in this study is a promising sensing material and will be widely used in the detection of toxic and harmful gas.

Supplementary Materials: The following supporting information can be downloaded at <https://www.mdpi.com/article/10.3390/chemosensors12010005/s1>, Figure S1: SEM images of sample S1–S4; Figure S2: Sensing responses of the sensor based on samples S1–S4 to 5.70 ppm of 2-CEES at different temperatures; Figure S3: Response of the sensor based on sample S2 to ammonia, ethanol, acetone and acetonitrile.

Author Contributions: Conceptualization, D.H. and S.W.; formal analysis, L.W., C.X., C.S., Y.Z. and W.Z.; investigation, C.X., C.S., Y.Z., X.G. and W.Z.; validation, L.Y., W.C., W.Y. and X.G.; writing—original draft, L.Y., W.C. and W.Y.; writing—review and editing, L.W., D.H. and S.W. All authors have read and agreed to the published version of the manuscript.

Funding: This work was supported by the National Natural Science Foundation of China (12004002), China Postdoctoral Science Foundation (2021M690996 and 2021M690995), Funds for scientific research activities of postdoctoral researchers in Anhui Province (2021B544 and 2021B492), and Foundation for Introduction of High-Level Talents of Anhui University (S020118002/061).

Institutional Review Board Statement: Not applicable.

Informed Consent Statement: Not applicable.

Data Availability Statement: The data presented in this study are available on request from the corresponding author.

Acknowledgments: We thank the Analytical and Testing Center of Anhui University for the characterization support. We would like to thank Yong Fan, Chenguang Qiu, and Kun Li for the experimental support.

Conflicts of Interest: All authors have given their approval for the final version of the manuscript and declare no competing financial interest.

References

1. Wang, Q.-Y.; Sun, Z.-B.; Zhang, M.; Zhao, S.-N.; Luo, P.; Gong, C.-H.; Liu, W.-X.; Zang, S.-Q. Cooperative catalysis between dual copper centers in a metal-organic framework for efficient detoxification of chemical warfare agent simulants. *J. Am. Chem. Soc.* **2022**, *144*, 21046–21055. [[CrossRef](#)] [[PubMed](#)]
2. Kumar, V.; Kim, H.; Pandey, B.; James, T.D.; Yoon, J.; Anslyn, E.V. Recent advances in fluorescent and colorimetric chemosensors for the detection of chemical warfare agents: A legacy of the 21st century. *Chem. Soc. Rev.* **2023**, *52*, 663–704. [[CrossRef](#)] [[PubMed](#)]
3. Liao, Y.; Song, J.; Si, Y.; Yu, J.; Ding, B. Superelastic and photothermal RGO/Zr-Doped TiO₂ nanofibrous aerogels enable the rapid decomposition of chemical warfare agents. *Nano Lett.* **2022**, *22*, 4368–4375. [[CrossRef](#)] [[PubMed](#)]
4. Fan, Y.; Li, K.; Ren, X.; Yan, W.; Zhu, C.; Zhao, Y.; Zeng, W.; Chen, Z.; Wang, S. A highly selective gas sensor based on the WO₃/WS₂ van der Waals heterojunction for the 2-chloroethyl ethyl sulfide (2-CEES) sensing application. *J. Mater. Chem. C* **2021**, *9*, 17496–17503. [[CrossRef](#)]
5. Majchrzak, T.; Wojnowski, W.; Lubinska-Szczygeł, M.; Róžańska, A.; Namieśnik, J.; Dymerski, T. PTR-MS and GC-MS as complementary techniques for analysis of volatiles: A tutorial review. *Anal. Chim. Acta* **2018**, *1035*, 1–13. [[CrossRef](#)] [[PubMed](#)]
6. Peng, L.; Jiang, D.; Wang, Z.; Hua, L.; Li, H. Dopant-assisted negative photoionization Ion mobility spectrometry coupled with on-line cooling inlet for real-time monitoring H₂S concentration in sewer gas. *Talanta* **2016**, *153*, 295–300. [[CrossRef](#)] [[PubMed](#)]
7. Jochum, T.; Rahal, L.; Suckert, R.J.; Popp, J.; Frosch, T. All-in-one: A versatile gas sensor based on fiber enhanced Raman spectroscopy for monitoring postharvest fruit conservation and ripening. *Analyst* **2016**, *141*, 2023–2029. [[CrossRef](#)]
8. Viespe, C. Development of Pd/TiO₂ Porous Layers by Pulsed Laser Deposition for Surface Acoustic Wave H₂ Gas Sensor. *Nanomaterials* **2020**, *10*, 760.
9. Haghighi, E.; Zeinali, S. Formaldehyde detection using quartz crystal microbalance (QCM) nanosensor coated by nanoporous MIL-101(Cr) film. *Microporous Mesoporous Mater.* **2020**, *300*, 110065. [[CrossRef](#)]
10. Lin, C.; Xian, X.; Qin, X.; Wang, D.; Tsow, F.; Forzani, E.; Tao, N. High Performance Colorimetric Carbon Monoxide Sensor for Continuous Personal Exposure Monitoring. *ACS Sens.* **2018**, *3*, 327–333. [[CrossRef](#)]
11. Mirzaei, A.; Ansari, H.R.; Shahbaz, M.; Kim, J.-Y.; Kim, H.W.; Kim, S.S. Metal Oxide Semiconductor Nanostructure Gas Sensors with Different Morphologies. *Chemosensors* **2022**, *10*, 289. [[CrossRef](#)]
12. Li, Y.; Liu, Y.; Lu, Y.; Liu, Z.; Sui, C.; Wang, Y.; Yang, L.; Liu, F.; Sun, P.; Liu, F.; et al. Preparation of BiOI-Functionalized ZnO Nanorods for Ppb-Level NO₂ Detection at Room Temperature. *ACS Sens.* **2022**, *7*, 3915–3922. [[CrossRef](#)] [[PubMed](#)]
13. Yang, J.; Yang, L.; Cao, S.; Yang, J.; Yan, C.; Zhang, L.; Huang, Q.; Zhao, J. High-performance metal-oxide gas sensors based on hierarchical core-shell ZnFe₂O₄ microspheres for detecting 2-chloroethyl ethyl sulfide. *Anal. Methods* **2023**, *15*, 3084–3091. [[CrossRef](#)] [[PubMed](#)]
14. Zheng, Q.; Wang, T.; Li, B.; Gao, R.; Zhang, X.; Cheng, X.; Huo, L.; Major, Z.; Xu, Y. Crosslinked WO₃ nanonet for rapid detection of sulfur mustard gas simulant: Mechanism insights and sensing application. *Sens. Actuators B Chem.* **2023**, *385*, 133704. [[CrossRef](#)]
15. Li, B.; Ma, X.; Xin, Y.; Major, Z.; Zhang, X.; Wang, T.; Huo, L.; Cheng, X.; Xu, Y. In situ construction of hierarchical Fe₂O₃ nanotube arrays for real-time detection and degradation of 2-CEES gas. *Sens. Actuators B Chem.* **2023**, *383*, 133590. [[CrossRef](#)]
16. Gui, Y.; Tian, K.; Liu, J.; Yang, L.; Zhang, H.; Wang, Y. Superior triethylamine detection at room temperature by {-112} faceted WO₃ gas sensor. *J. Hazard. Mater.* **2019**, *380*, 120876. [[CrossRef](#)] [[PubMed](#)]
17. Recum, P.; Hirsch, T. Graphene-based chemiresistive gas sensors. *Nanoscale Adv.* **2024**. [[CrossRef](#)] [[PubMed](#)]
18. Wang, X.; Cao, R.; Zhang, S.; Hou, P.; Han, R.; Shao, M.; Xu, X. Hierarchical flowerlike metal/metal oxide nanostructures derived from layered double hydroxides for catalysis and gas sensing. *J. Mater. Chem. A* **2017**, *5*, 23999–24010. [[CrossRef](#)]
19. Sun, B.; Qin, F.; Jiang, L.; Gao, J.; Liu, Z.; Wang, J.; Zhang, Y.; Fan, J.; Kan, K.; Shi, K. Room-temperature gas sensors based on three-dimensional Co₃O₄/Al₂O₃@Ti₃C₂T_x MXene nanocomposite for highly sensitive NO_x detection. *Sens. Actuators B Chem.* **2022**, *368*, 132206. [[CrossRef](#)]

20. Meng, F.; Yuan, Z.; Meng, D. Chemical sensors for volatile organic compound detection. *Chemosensors* **2023**, *11*, 553. [[CrossRef](#)]
21. Jo, Y.-M.; Jo, Y.K.; Lee, J.-H.; Jang, H.W.; Hwang, I.-S.; Yoo, D.J. MOF-Based Chemiresistive Gas Sensors: Toward New Functionalities. *Adv. Mater.* **2023**, *35*, 2206842. [[CrossRef](#)] [[PubMed](#)]
22. Patil, L.A.; Deo, V.V.; Shinde, M.D.; Bari, A.R.; Kaushik, M.P. Sensing of 2-chloroethyl ethyl sulfide (2-CEES)—A CWA simulant—Using pure and platinum doped nanostructured CdSnO₃ thin films prepared from ultrasonic spray pyrolysis technique. *Sens. Actuators B Chem.* **2011**, *160*, 234–243. [[CrossRef](#)]
23. Yoo, R.; Lee, D.; Cho, S.; Lee, W. Doping effect on the sensing properties of ZnO nanoparticles for detection of 2-chloroethyl ethylsulfide as a mustard simulant. *Sens. Actuators B Chem.* **2018**, *254*, 1242–1248. [[CrossRef](#)]
24. Aliha, H.M.; Khodadadi, A.A.; Mortazavi, Y. The sensing behaviour of metal oxides (ZnO, CuO and Sm₂O₃) doped-SnO₂ for detection of low concentrations of chlorinated volatile organic compounds. *Sens. Actuators B Chem.* **2013**, *181*, 637–643. [[CrossRef](#)]
25. Patil, L.A.; Deo, V.V.; Shinde, M.D.; Bari, A.R.; Patil, D.M.; Kaushik, M.P. Improved 2-CEES sensing performance of spray pyrolyzed Ru-CdSnO₃ nanostructured thin films. *Sens. Actuators B Chem.* **2014**, *191*, 130–136. [[CrossRef](#)]
26. Horsfall, L.A.; Pugh, D.C.; Blackman, C.S.; Parkin, I.P. An array of WO₃ and CTO heterojunction semiconducting metal oxide gas sensors used as a tool for explosive detection. *J. Mater. Chem. A* **2017**, *5*, 2172–2179. [[CrossRef](#)]
27. Ou, L.-X.; Liu, M.-Y.; Zhu, L.-Y.; Zhang, D.W.; Lu, H.-L. Recent Progress on Flexible Room-Temperature Gas Sensors Based on Metal Oxide Semiconductor. *Nano-Micro Lett.* **2022**, *14*, 206. [[CrossRef](#)]
28. Liu, Y.; Su, C.; Chen, X.; Li, B.; Jiang, W.; Zeng, M.; Hu, N.; Su, Y.; Zhou, Z.; Zhu, Z.-g.; et al. Hierarchical WS₂-WO₃ Nanohybrids with P-N Heterojunctions for NO₂ Detection. *ACS Appl. Nano Mater.* **2021**, *4*, 1626–1634.
29. Yang, Z.; Li, B.; Han, Y.; Su, C.; Chen, X.; Zhou, Z.; Su, Y.; Hu, N.; Zhang, Y.; Zeng, M. Gas sensors based on two-dimensional transition metal dichalcogenide nanoheterojunctions. *SciEngine* **2019**, *64*, 3699–3716.
30. Ren, Y.; Zou, Y.; Liu, Y.; Zhou, X.; Ma, J.; Zhao, D.; Wei, G.; Ai, Y.; Xi, S.; Deng, Y. Synthesis of orthogonally assembled 3D cross-stacked metal oxide semiconducting nanowires. *Nat. Mater.* **2020**, *19*, 203–211. [[CrossRef](#)]
31. Yuan, H.; Aljneibi, S.; Yuan, J.; Wang, Y.; Liu, H.; Fang, J.; Tang, C.; Yan, X.; Cai, H.; Gu, Y.; et al. ZnO Nanosheets Abundant in Oxygen Vacancies Derived from Metal-Organic Frameworks for ppb-Level Gas Sensing. *Adv. Mater.* **2019**, *31*, e1807161. [[CrossRef](#)] [[PubMed](#)]
32. Lee, J.; Jung, Y.; Sung, S.-H.; Lee, G.; Kim, J.; Seong, J.; Shim, Y.-S.; Jun, S.C.; Jeon, S. High-performance gas sensor array for indoor air quality monitoring: The role of Au nanoparticles on WO₃, SnO₂, and NiO-based gas sensors. *J. Mater. Chem. A* **2021**, *9*, 1159–1167. [[CrossRef](#)]
33. Chan, N.Y.; Zhao, M.; Huang, J.; Au, K.; Wong, M.H.; Yao, H.M.; Lu, W.; Chen, Y.; Ong, C.W.; Chan, H.L.; et al. Highly sensitive gas sensor by the LaAlO₃/SrTiO₃ heterostructure with Pd nanoparticle surface modulation. *Adv. Mater.* **2014**, *26*, 5962–5968. [[CrossRef](#)] [[PubMed](#)]
34. Zhu, X.; Guo, Y.; Ren, H.; Gao, C.; Zhou, Y. Enhancing the NO₂ gas sensing properties of rGO/SnO₂ nanocomposite films by using microporous substrates. *Sens. Actuators B Chem.* **2017**, *248*, 560–570. [[CrossRef](#)]

Disclaimer/Publisher’s Note: The statements, opinions and data contained in all publications are solely those of the individual author(s) and contributor(s) and not of MDPI and/or the editor(s). MDPI and/or the editor(s) disclaim responsibility for any injury to people or property resulting from any ideas, methods, instructions or products referred to in the content.